Dyes and Pigments 199 (2022) 110071

Contents lists available at ScienceDirect

Dyes and Pigments

journal homepage: www.elsevier.com/locate/dyepig

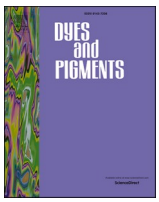

Benzodifuran-based fluorescent brighteners: A novel platform for plant cell wall imaging

Rosita Diana [a], Ugo Caruso [b], Francesco Silvio Gentile [b], Luigi Di Costanzo [a], David Turrà [a,c], Stefania Vitale [a,1], Barbara Panunzi [a,*]

[a] Department of Agricultural Sciences, University of Naples Federico II, Portici, NA, Italy
[b] Department of Chemistry, University of Naples Federico II, Napoli, Italy
[c] Center for Studies on Bioinspired Agro-enviromental Technology, Università di Napoli Federico II, Portici, NA, Italy

ARTICLE INFO

Keywords:
Fluorescent brightener agents
Plant cell wall
Bioimaging
Microscopy

ABSTRACT

Herein we designed three novel fluorescent brightening agents based on a benzodifuran skeleton. The compounds are colorless fluorophores emitting in the blue region with an improved water solubility and ability to interact with living cells. A complete understanding of the emission mechanisms was achieved by Density Functional Theory study based on X-ray crystallographic analysis. The fluorescence quantum yields were measured in different solvents and at different pH values. The ability of the different fluorophores to stain cell compartments of plant root samples was tested in water- and glycerol-based solutions. Through fluorescence microscopy technique two probes with a different functionalized branching chain proved to be efficient stains for plant root cell wall. The cationic probe has no harmful effect on plant tissues and is suitable for in vivo fluorescent visualization of plant root cell boundaries. This study sheds light on the potential use of brighteners containing a central benzodifuran core as tools for imaging of fixed and alive plant tissues.

1. Introduction

Synthetic fluorescent dyes for targeted applications have been used by biologists for decades. In the past fifty years several examples of fluorophores specifically designed as sensors and markers have become commercially available, and the recent abundance of patents proves the economic impact of the research in this field [1–6]. Compounds known as fluorescent brightener agents (FBAs), also called fluorescent whitening agents (FWAs) have been consigned to the textile and pigment industry for years [7–9]. These additives are also used in the solid state as to cause a "whitening" effect and to enhance the color appearance of fabric, plastic, and paper [10]. Specifically, FBAs are colourless compounds able to absorb light in the ultraviolet region (in a typical range of 340–370 nm) of the electromagnetic spectrum, and emit fluorescent light in the blue region (typically 420–470 nm). They often benefit from good solubility, high fluorescence quantum yield, and functional groups able to bind to target analytes and/or sites. More recently researchers acquired interest in their use as markers and/or sensors for biological substrates and promoted them as tools for microscope analysis [11–13].

Fluorescence microscopy has been widely used in visualizing both immotile cellular compartments and highly dynamic molecular processes in living organisms within single-cell or at a whole-tissue/organism level [14,15]. This technique is capable of delivering accurate information on biological processes or states with spatio-temporal resolution both in the wide-field mode (*e.g.* epifluorescence) or by using point detection (*e.g.* laser scanning confocal microscopy) [16,17]. Several of the fluorophores commonly used with this imaging technique emit in the red, green, and blue (RGB model [18]) visible region of the electromagnetic spectrum; among them, FBAs are tools worth to note. The fundamental idea of using FBAs in different microscopy configurations is to obtain fluorescent biomarkers brightening up with a sharp contrast from dark background of the cell or of its specific compartments [19].

The plant cell wall represents the rigid skeleton of plants and the main component of wood [20,21]. Structurally, plant cell walls are formed by a complex mesh of macromolecules primarily comprising polysaccharides polymers such as cellulose, hemicellulose, and pectin, often including lignin and glycoproteins. Despite most plant cell walls

* Corresponding author.
E-mail address: barbara.panunzi@unina.it (B. Panunzi).
[1] Current address: Institute for Sustainable Plant Protection, National Research Council, 80,055 Portici, Italy.

https://doi.org/10.1016/j.dyepig.2021.110071
Received 8 October 2021; Received in revised form 26 November 2021; Accepted 26 December 2021
Available online 31 December 2021

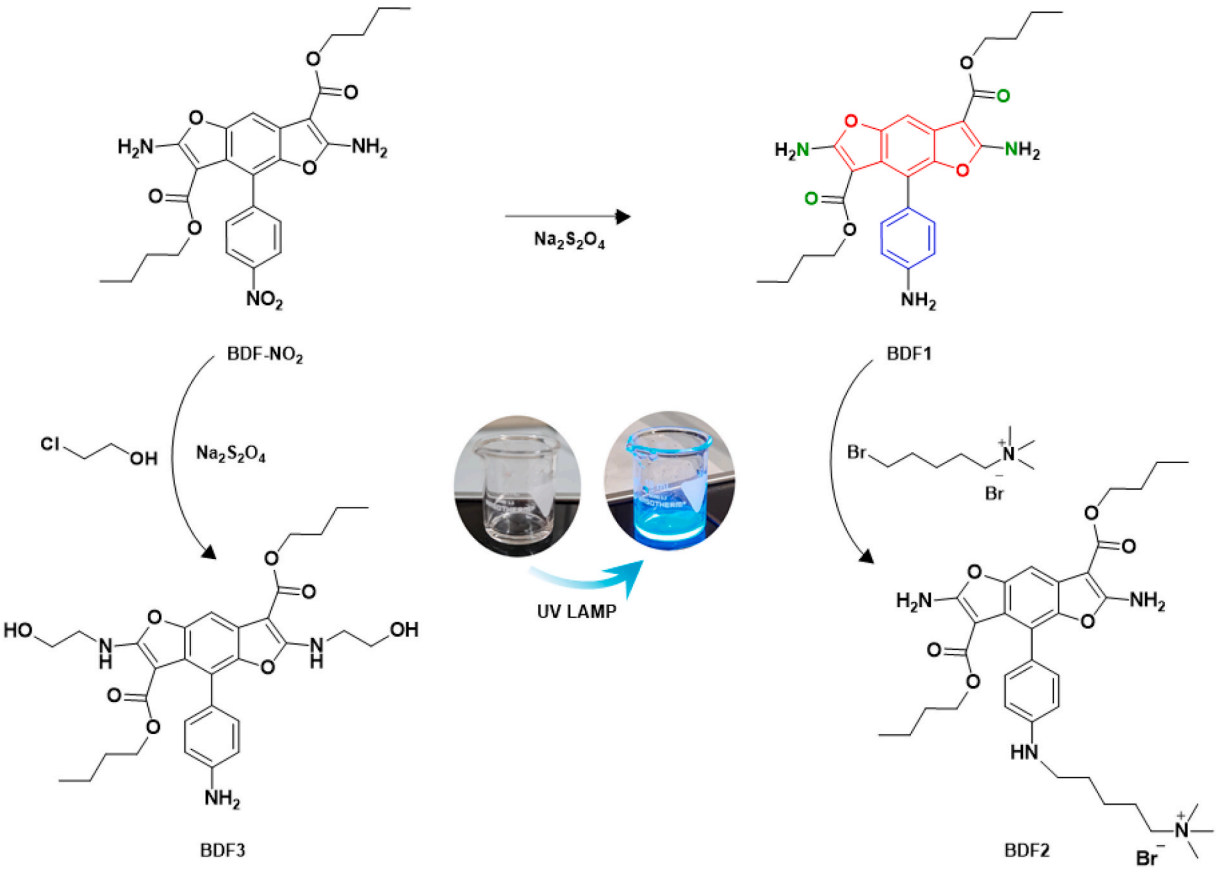

Scheme 1. Synthetic route for probes BDF1, BDF2 and BDF3 (BDF main plane in red). In blue is marked the phenyl ring (rotated respect to the main plane) and in green the atom groups involved in the H bond. In the inset: a DMSO solution 1.0 mM of BDF2 in natural light and under a standard UV-lamp (365 nm).

have cellulose as their major structural and functional constituent, their highly dynamic and heterogeneous structure allows plant cells to have different morphologies, sizes and physicochemical properties depending on the specific cell type [22–25]. Small fluorescent molecules able to recognize specific cell wall are highly desirable for fluorescence microscopy to study cell wall architecture and dynamics at the molecular scale [26–28]. Such markers are required to have functional groups potentially interacting with plant cell wall molecules, high emission strength and brightness, good transparency, lightfastness properties, stability, and good cell permeability. In addition, a non-invasive and non-destructive interaction of the fluorescent probes with the living cell can be desirable to track plant cell wall morphological and developmental alterations in vivo over time. The commercial fluorophore Calcofluor White M2R (CFW, or FBA 18), which is used by the early 1940s, represents a well-known example of an FBA with such characteristics. Due to its brilliant bluish-white emission under UV light ($\lambda_{em} = 475$ nm) and the high water-solubility (>10 mg/mL) this stilbene-based FBA is commonly used as a staining agent for fungal, bacterial, algal and higher plant cells [29]. Notably, these types of fluorescent probes are of a special interest for live-cell imaging due to their water solubility, brightness, photostability, low cytotoxicity and cell permeability [30,31].

Among the conspicuous diversity of FBAs chemical structures, the large family of heterocyclic compounds includes many examples of fluorescence markers. Heterocycle molecules containing oxygen atom group(s) exhibit optical, biological, and pharmacological activity due to their similarity to several natural bioactive molecules [32,33]. In this context, benzofuran derivatives as electron-rich building blocks proved to be excellent photoluminescent materials [34–36] with interesting biological properties including antimicrobial and antifungal [37–39], antitumor [40,41], anti-parasitic [42], anti-inflammatory [43], and analgesic activity [44]. Specifically, benzodifuran (BDF) rings are potential fluorescent molecules [45] easily obtainable by reaction of 1,4-benzoquinone with a cyanoacetic ester in alcoholic ammonia [46–48]. The ring closure reaction leads to functionalized derivatives where the choice of the substituents can tune the solubility in organic and aqueous media.

For this study, we used a facile two-steps synthetic route to obtain a benzodifuran core (BDF-NO_2 in Scheme 1) from 2-(4-nitrophenyl)-1,4-benzoquinone and butylcyanoacetate with subsequent reduction reaction of the nitro functional group to obtain BDF1 molecule in Scheme 1. Compounds BDF2 and BDF3 in Scheme 1 are of BDF1 by insertion of different functionalized branching chains on the aminic nitrogen atom groups. All compounds BDF1-3 are colorless FBAs emitting in the blue region. Compounds BDF2 and BDF3 were specifically designed to improve the solubility in an aqueous medium and to interact with living cells.

The fluorophores were characterized as for their chemical, structural and optical behavior. The fluorescence quantum yields (PLQYs) were measured in different solvents and the influence of the pH parameter was evaluated. For a full characterization of the probes, a theoretical DFT analysis was performed using BDF1 X-ray crystal structure analysis to ascertain the underlying mechanisms of fluorescence at the molecular level. Finally, BDF2 and BDF3 were used in biological studies to verify the effectiveness of the probes on plant cell wall substrates. Tests were carried out on two-week-old seedlings of Tomato (cultivar S. Marzano nano), a model crop plant used in biological studies ranging from the molecular to the morphological approach [49–52]. Epifluorescence as the simplest, most versatile, and widely employed application of fluorescence microscopy [53] was used to investigate BDF2 and BDF3 fluorescence on thick plant root samples (~150–300 μm diameter) either in a water- or a glycerol-based solvent, the latter used as a

viscosity-activated fluorescence booster [54–56].

2. Experimental parts

Commercially available starting materials were supplied by Sigma Aldrich. The compound 2,6-diamino-4-(4-nitrophenyl)benzo[1,2-b:4,5-b']difuran-3,7-dicarboxylate (BDF) was obtained as previously described [45]. ^{1}H NMR spectra were recorded in DMSO-d_6 with a Bruker Advance II 400MHz apparatus (Bruker Corporation, Billerica, MA, USA). Mass spectrometry measurements were performed using a Q-TOF premier instrument (Waters, Milford, MA, USA) with an electrospray ion source and a hybrid quadrupole-time of flight analyzer. Optical observations of the phase transitions were performed by using a Zeiss Axioscop polarizing microscope (Carl Zeiss, Oberkochen, Germany) equipped with an FP90 Mettler microfurnace (Mettler-Toledo International INC MTD, Columbus, OH, USA). The decomposition temperatures (5 wt% weight loss) and phase transition temperatures and enthalpies were measured under nitrogen flow by employ of a DSC/TGA PerkinElmer TGA 4000 (PerkinElmer, Inc., Waltham, MA, USA), scanning rate 10 °C/min. Absorption and UV–Visible emission spectra were recorded by JASCO F-530 and FP-750 spectrometers (scan rate 200 nm/min, JASCO Inc., Easton, MD, USA) and on a spectrofluorometer Jasco FP-750 (excitation wavelengths set at the absorption maxima of the samples, scan rate 125 nm/min, JASCO Inc., Easton, MD, USA). Thin films of the neat samples were prepared using a SCS P6700 spin coater operating at 600 RPM for 1 min. Photoluminescence quantum efficiency values were recorded on quartz substrates by a Fluorolog 3 spectrofluorometer (Horiba Jobin Instruments SA), within an integrating sphere provided by an optical fiber connection. In solution, PLQYs were calculated in ethanol/water (1:1) diluted solutions below absorbance 0.20, according to Melhuish. Positive Reflectron MALDI spectra were recorded on an AB Sciex TOF/TOF 5800 instrument using 2,5-dihydroxybenzoic acid as the matrix.

2.1. Synthetic procedures

2.1.1. Synthesis of BDF1

An amount of 0.509 g of BDF-NO_2 (1.00 mmol), dispersed in 100 mL of ethanol and water 1:1, was added to 0.696 g $Na_2S_2O_4$ (4.00 mmol). The mixture was stirred and refluxed for 4 h. Then, the ethanol was removed from the solution under vacuum, by cooling the aqueous solution, the product precipitated at room temperature. The compound was recovered by filtration and washed twice in water. As result a whitish solid was obtained and dried at 80 °C under vacuum. Yield: 70%. The product was then bicrystallised from ethanol/water (2:1). Mp = 230 °C. Td = 270 °C.

^{1}H NMR (400 MHz, DMSO-d_6, 25 °C): δ = 7.55 (s, 4H), 7.27 (s, 1H), 7.01 (d, 2H), 6.62 (d, 2H), 5.38 (s, 2H), 4.23 (t, 2H), 3.62 (t, 2H), 1.72 (m, 2H), 1.44 (m, 2H) ppm, 1.07 (m, 4H), 0.961 (m, 3H), 0.790 (m, 3H). MALDI-TOF of BDF1 m/z: 502 ($M+Na^+$). Elemental analysis calculated (%) for $C_{26}H_{29}N_3O_6$: C, 65.12; H, 6.10; N, 8.76; found: C, 65.60; H, 6.42; N, 8.60.

2.1.2. Synthesis of BDF2

For the preparation of BDF2, the precursor BDF1 (0.479 g, 1.00 mmol), dissolved in 25 mL of acetone, was added to 0.578 g of (5-bromopentyl) trimethylammoniumbromide (2.00 mmol) and 0.300 g of K_2CO_3. The reaction was stirred at reflux for 3 h. Then, the suspension was cooled and the solid removed by filtration. The solution was dried under vacuum and the precipitate crystallized from methanol/ether. A whitish solid was obtained and dried at 80 °C under vacuum and the yield evaluated as 60%. The product was then bicrystallised from ethanol/water. Mp = 206 °C, melting with decomposition.

^{1}H NMR (400 MHz, DMSO-d_6, 25 °C): δ = 7.60 (d, 4H), 7.29 (s, 1H), 7.08 (dd, 4H), 6.65 (s, 1H), 4.23 (m, 2H), 3.58 (m, 4H), 3.29 (m, 2H), 3.04 (m, 9H), 1.86 (m, 2H), 1.72 (m, 4H), 1.45 (m, 4H), 1.06 (m, 4H), 0.96 (m, 3H), 0.78 (m, 3H) ppm. MALDI-TOF of BDF2 m/z: 607 ($M-Br^-$). Elemental analysis calculated (%) $C_{34}H_{47}N_4O_6Br$: C, 59.38; H, 6.89; N, 8.15; found: C, 59.76; H, 6.43; N, 8.34.

2.1.3. Synthesis of BDF3

The precursor BDF-NO_2 (0.509 g, 1.00 mmol), dissolved in 25 mL of THF, was added to 0.322 g of 2-chloroethan-1-ol (4.00 mmol) and 0.600 g of K_2CO_3. The reaction was stirred at reflux for 4 h. Then, the suspension was cooled and the solid removed by filtration. Cooled the solution, the product precipitated at room temperature. A whitish solid was obtained by filtration and crystallized from acetone. The subsequent reduction of nitro to amino group for the synthesis of BDF3 was carried out with the same synthetic procedure as BDF1. A whitish solid was obtained and dried at 80 °C under vacuum with yield of 65%. The product was then bicrystallised from ethanol/water. Mp = 197 °C. Td = 220 °C.

^{1}H NMR (400 MHz, DMSO-d_6, 25 °C): δ = 7.55 (dd, 4H), 7.27 (s, 1H), 7.07 (d, 2H), 6.71 (s, 2H), 4.22 (t, 2H), 3.61 (t, 2H), 3.41 (m, 8H), 1.72 (m, 2H), 1.44 (m, 2H), 1.08 (m, 4H), 0.943 (m, 3H), 0.784 (m, 3H) ppm. MALDI-TOF of BDF3 m/z: 590 ($M+Na^+$). Elemental analysis calculated (%) $C_{30}H_{37}N_3O_8$: C, 63.48; H, 6.57; N, 7.40; found: C, 63.20; H, 6.63; N, 7.22.

2.2. Single-crystal X-ray analysis

Crystals of BDF1 were obtained at room temperature by slow evaporation from an ethanol solution (about 500 μM, 2 mL) of the compound not yet subjected to bicrystallization. White-yellow crystals of BDF1 complex appeared as plates with typical dimensions of 0.3x0.4 × 0.3 mm. Data were collected with synchrotron radiation (wavelength, 0.7000 Å) from XRD1 beamline at the Elettra Synchrotron Light Source, Trieste Italy. By using a small loop of fine rayon fiber, selected crystal for data diffraction was dipped in cryoprotectant Paratone oil and flash-frozen in a stream of nitrogen at 100 K. For the best diffracting crystal, a total of 400-degree crystal rotation data were collected using an oscillation range of 0.5°. Data were processed using XDS and POINTLESS 1.11.21 with data collection statistic reported in Table S1 [57,58]. Crystals have an orthorhombic unit cell with axes a = 16.77 Å, b = 8.51 Å, c = 34.14 Å, V = 4874 Å^3 and space group *P* n a 2_1. No data twinning was detected. Structure solution was found by direct methods using SHELXS [59] which revealed the expected BDF1 skeleton corresponding to two distinct molecules in the ASU. Structure was anisotropically refined using full matrix least-squares methods on F^2 against all independent measured reflections using SHELXL [60] run under WinGX suite for the refinement of small molecules [61]. Although the ester n-butyl groups are visible aliphatic chains are disordered and refined as unrestrained groups. Two residual peaks in difference electron density map were observed for one the BDF1 molecules. These peaks were interpreted as corresponding to oxygen atoms of the nitro group of the starting material. These atoms were refined with an occupancy of 0.5 each, thus representing ~13% of unreacted compound. Hydrogen atoms were introduced and refined in agreement with a riding model as implemented in SHELXL. Crystal data and structure refinement details for BDF1 are reported in Table S1. Figures were generated using Mercury CSD 3.6 [62] Crystallographic data for BDF1 have been deposited with the Cambridge Crystallographic Data Centre and can be obtained via www.ccdc.cam.ac.uk/data_request/cif.

2.3. Molecular modelling

Ab initio calculation adopting Density Functional Theory (DFT) and Time Dependent Density Functional Theory (TD-DFT) formalisms were performed for the analysis of ground and excited state of BDF1 system, adopting hybrid functionals and a large basis set. The guess input structure of a molecular model of BDF1 were extracted from the X-ray crystal structure. An exhaustive description of the computational details

Table 1
Absorption and emission properties of BDF1-3 measured in water, glycerol, and in DMSO solutions.

Sample	λ_{abs} [a]			e·10^3 [M^{-1}cm^{-1}]	λ_{em} [b]			CIE	PLQY% [c]		
	water	glycerol	DMSO	DMSO	water	glycerol	DMSO	DMSO	water	glycerol	DMSO
BDF1	275	279	280	34.6	426	427	421	0.22;0.31	1.2	2.0	26
BDF2	273	274	281	29.7	420	422	421	0.22;0.30	1.2	3.1	32
BDF3	273	275	280	30.1	421	421	420	0.21;0.30	2.5	3.2	25

a) Wavelength of UV–Visible absorbance maxima (and related molar extinction coefficients measured in DMSO); b) Wavelength of emission maxima (and related CIE coordinates measured in DMSO); c) relative PLQYs.

was previously reported [63–65], and it has been summarily featured in the Supplementary Material. In this kind of organic brightener, the combination of global hybrid DFT functional with large basis set provides a good agreement with experimental data.

The relaxed geometrical structure in the gas phase (after optimization through the analytical gradient evaluation) was employed as starting point for HOMO-LUMO orbital characterization. The simulated absorption spectrum was obtained by TD-DFT simulation. Following gradient optimization of the first root of the excited states, the emission peak in the fluorescence spectra was predicted. Plots of the orbital and the electronic density (differential and natural transition orbitals) were produced and discussed in Section 3.3.

2.4. Plant growth conditions

Tomato seeds (cultivar S. Marzano nano, provided by La Semiorto Sementi) were surface sterilized by soaking them for 20 min in a solution of 20% commercial bleach. Surface-sterilized seeds were washed three times with sterile bidistilled water and seeded in sterile vermiculite. Plants were maintained in a growth chamber (15/9 h light/dark photoperiod, 28 °C) until they reached the second true leaf stage. Seedlings were carefully explanted, roots washed thoroughly to remove the attached vermiculite, appropriately treated (see below) and observed under a fluorescence microscope.

2.5. Preparation of plant material for fluorescence microscopy

Fresh tomato roots were rinsed twice with sterile distilled water, submerged in sterile water in a 90 mm Glass Petri Dish and 1 mm to 1 cm long segments or transversal hand-sections were obtained by using a disposable razor blade. Plant tissues were then transferred for one or 2 h into Eppendorf tubes either containing 500 μL of the staining solution or of the solvent control solution, including the same reagents except the dye. BDF2 and BDF3 stock solutions were prepared by dissolving the dye in water with 4% ethanol (water-based solution) and glycerol with 1% DMSO (glycerol-based solution) at 1 mM. The stock solutions were diluted to 500 μM, 100 μM and 10 μM concentrations with water.

Plant segments previously treated with staining or control solutions were washed twice with the solvent control solution and either imaged directly or stained for 10 min with 300 ng/mL propidium iodide (PI by Sigma Aldrich) and immediately mounted in water to test for cell viability. For plant cell wall staining, root segments were immersed in 1 mL of 470 nM Calcofluor White (CFW by Sigma Aldrich) for 10 min, rinsed twice with sterile dd H_20 and imaged. Wide-field fluorescence imaging was performed with an Axioskop2 Plus microscope equipped with a Zeiss AxioCam HRc digital camera (Zeiss, Milan, Italy), using a × 10 magnification objective and the following filter blocks: CFW, BDF3 staining (BP 365/12, FT 395, LP 397), PI staining (BP 546/12, FT 580, LP 590) and BDF2 staining (BP 350/50, FT 395, LP 397). Micrographs were captured by using the Axiovision 4.8 software (Zeiss). Measurement of fluorescence intensity and normalization of mean root fluorescence intensity in stain-treated samples relative to that of control treated roots was performed by using the ImageJ software [66]. All experiments were performed at least three times on two or more independent occasions.

3. Results and discussions

3.1. Design and fluorescence performance of BDF1-3

The synthetic route for the precursor BDF-NO_2 (dibutyl 2,6-diamino-4-(4-nitrophenyl)benzo[1,2–4,5-]difuran-3,7-dicarboxylate in Scheme 1) [45] followed the reported procedure of diazotization of 4-nitroaniline and coupling on benzoquinone. The reduction reaction of BDF-NO_2 with $Na_2S_2O_4$ provides the FBA molecule named BDF1. Identification and purity degree evaluation of all products were assessed by elemental analysis, mass spectrometry and ^{1}H NMR. The FBAs named BDF1-3 were obtained at about 95% purity degree by two consecutive crystallizations in ethanol/water.

The cruciform structure of the three FBAs shows a high extent of conjugation and planarity along the BDF main plane (marked in red in Scheme 1 for BDF1). As previously noted, two non-equivalent sides of the molecule are recognizable in all derivatives [34] of similar structures. Specifically, a more encumbered side is due to the concomitant presence of a phenyl group (marked in blue in Scheme 1 for BDF1) and a butyl ester group. The ^{1}H NMR spectrum shows splitted resonances (see Section 2.1) clearly confirming the non-equivalence of the two sides. On both sides of the BDF1-3 molecules the aminic nitrogen on the BDF main plane (marked in green in Scheme 1 for BDF1) undergo an intramolecular H-bond (see Section 3.2) with the oxygen in the C═O group of the butyl substituents (marked in green in Scheme 1 for BDF1). The intermolecular interaction contributes to stiffen the BDF main plane. The "steady" intramolecular H-bond and the presence of the butyl substituents produce hindrance to the virtually free-rotating parts of the molecule [67–70]. The dynamic intramolecular rotations are expected to cause a fluorescence quenching by dissipating the exciton energy [67,69,71]. Therefore, the RIR (restriction of intramolecular rotations) effect [72] and the electronic pattern established in our FBAs (Section 3.3) must be considered contributing factors to the emission recorded both in solution and on the powder samples. As expected, also the neat solid sample BDF1-3 shows a mild whitish-blue emission under an UV–vis lamp at 365 nm. Their PLQYs (photoluminescence quantum yields) in the solid-state ranges from 5% to 7%.

The compounds BDF2 and BDF3 are analogous to BDF1 purposefully designed to improve the solubility and fluorescence response in biological samples. Considering CFW functional groups, a cationic chain was added to maximize the water solubility in BDF2, while the ethanolic chains in BDF3 were added to improve interaction with the hydroxyl groups of plant cell wall components (e.g. cellulose, hemicellulose). As expected, the cationic probe BDF2 is the most soluble in water (8 mg/mL) followed by BDF3 (5 mg/mL) and finally BDF1 (2 mg/mL).

In solution, the FBAs underwent a full spectroscopic analysis by absorption and UV–Visible emission spectrophotometry employing water, DMSO, ethanol, and glycerol solutions. All the solutions of BDF1-3 are stable and retain their spectroscopic characteristics up to three months under natural light at room temperature. Absorbance and emission data are summarised in Table 1 and the spectra recorded in DMSO solvent for BDF1-3 are reported in Figs. S1–3 as an example of their similarity.

In different solvents the absorbance/emission pattern is mostly retained, though the emission intensities are enhanced in organic

solvents such as DMSO and in glycerol. The general absorbance pattern of the FBAs in solution reveals a main broad band (peaked at 275 nm for BDF1 and at 273 nm for BDF2-3) with a shoulder at about 320 nm. The emission spectrum of the same samples irradiated at the absorbance maximum shows a single band (peaked at 426 nm for BDF1, at 420 nm for BDF2 and 421 nm for BDF3, respectively). Remarkably large (about 150 nm) Stokes shifts are recorded in all cases, confirming the desirable non-overlapping of absorbance and emission bands (see also Figs. S1–3) [73,74]. CIE coordinates measured for the emission of BDF1 in solution are (0.22; 0.31). For BDF2 and BDF3 CIE coordinates are nearly identical (see Table 1), as expected for the same fluorophore core.

PLQYs were measured in water, glycerol and DMSO (Table 1). PLQYs in aqueous media range from 1 to 3.2%. PLQYs measured in DMSO increases approximately 10 times, reaching the significant value of 32% for the cationic derivatives BDF2. Although the quantum yields measured in polar protic solvents are not noteworthy, it should be noted that the probes can give a neat and bright signal by interacting with the functional groups of the cell wall constituents, as will be discussed in Section 3.4. The factors contributing to fluorescence emission spectra and quantum yields include solvent polarity, interaction solvent-fluorophore, viscosity, and pH among other factors [75]. As expected, fluorescence emission intensity is lower in polar protic solvents potentially interacting with the fluorophore [76]. Polar solvent molecules surrounding the fluorophore interact with the dipole moment or through H-bond formation, yielding an ordered distribution of solvent molecules around the fluorophore. The solvent effect can decrease the energy of the excited state and increases the possibility of excimer formation, with both effects of shifting the emission maxima and decreasing emission intensity [77]. In our case, the effect of the solvent on the emission maxima is negligible (see Table 1). Contrarly, the different emission intensity can be ascribed to a relevant effect of the solvent polarity on the excited state population. Specifically, the effect is related with the stabilization of the excimer geometry and the reduction of the energetic barrier to excimer formation [78]. Another relevant parameter is the viscosity of the solvent. Glycerol is a useful solvent that enhances the emission efficiencies due to its turbid characteristic [79]. The local higher density increases the local refractive index and, therefore, enhances the brightness of the fluorophore [80]. Based on these observations, different performances depending on the solvent could be expected for BDF2 and BDF3 in staining cell wall.

Finally, the excited-state intramolecular proton transfer (ESIPT) process has been considered potentially occurring in our FBAs, due to the tautomeric keto-enolic equilibrium. The equilibrium could involve the transfer of the intramolecular proton from the nitrogen atom group to the oxygen atom group (marked in green in Scheme 1 for BDF1) in one or both sides of the molecule. Most of the ESIPT fluorophores shows dual emission: a short wavelength emission due to the excited state enol form and a longer emission due to the excited state keto form (ESIPT emission). The process generates different transient species easily affected by the microenvironment. Therefore, ESIPT probes easily undergo changes in the fluorescence properties depending on the acidity/basicity and functional groups of the surrounding medium [81]. Contrarily to other BDF derivatives previously explored by us [34], the FBAs examined in this study not undergo a solvent-assisted ESIPT process (see Section 3.3). In this context, pH could be a relevant parameter. We tested the relevance of pH by recording the absorption and emission spectra of BDF1-3 in buffered water solutions at pH 4.8, 6.5 and 7.8. While in highly acidic solutions (pH $<$ 3) the fluorescence signal decreases by half, and turbidity is produced above pH $=$ 9, the absorption and fluorescence spectra resulted unchanged within the pH range 5–8. For our study, the advantage of a pH-independent probe lies in the fluorescent intensity not affected by the environment in the range of use for plant cell staining (about 5–7.8) [82,83].

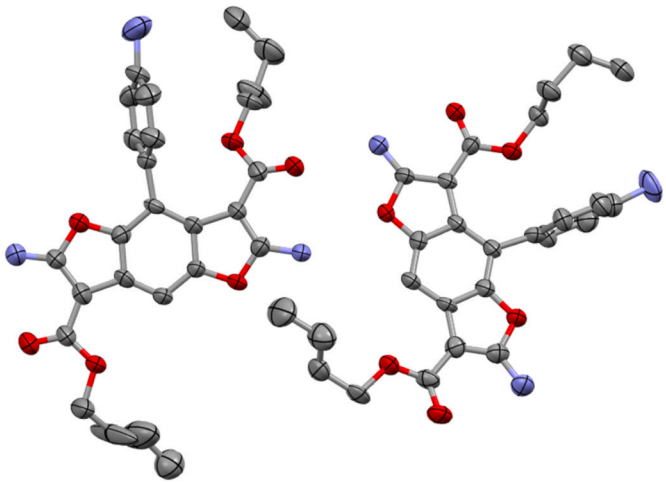

Fig. 1. Thermal ellipsoids representation of BDF1 dimer drawn at 50% probability. Atoms are color-coded as follows: carbon (gray), oxygen (red), nitrogen (blue).

3.2. X-ray structural characterization of BDF1

Crystals of BDF1 were obtained by slow evaporation at room temperature (see Section 2.6). The asymmetric unit contains two molecules of BDF1 as shown in Fig. 1. The structure of BDF1 consists of the benzodifuran plane branched with two amino groups, and an aminophenyl group. This group is twisted with respect mean average plane of the benzodifuran and the angle between the two mean planes is ~74°. The amino groups of the benzodifuran lay on the mean plane of the BDF central core and the overall *rmds* of the atoms with respect the mean plane is ~0.06 Å. Each molecule of BDF1 is stabilized by two intramolecular hydrogen bonds (average distance is 2.85 Å) involving each of the benzodifuran amino groups as atom donor and the oxygen atom group (acceptor atom) not involved in the ester bond (intramolecular and intermolecular hydrogen bonds interactions are shown in Fig. S4). In agreement with the symmetry elements of *P* n a 2_1 space-group the crystal packing shows a jigsaw puzzle arrangement of BDF1 molecule in such a way to stabilize intermolecular hydrogen bonds involving the amino groups and oxygen atom groups of the ester. Finally, several intermolecular Van-der Waals interactions involving the aliphatic groups of the n-butyl chains and the aminophenyl group are observed.

3.3. DFT analysis of BDF1-3

DFT calculations were performed from molecular cluster extracted from X-ray crystallography of BDF1. The molecular cluster were relaxed through minimization of the electron density gradient. The keto-enolic tautomeric equilibrium process evaluated by the energy of three different tautomers: the ketonic molecule, the single enolic form (by single proton transfer, on one side of the molecule) and the double enolic form (by double proton transfer, on both side of the molecule). The protonic transfers order was determined based on the distance, although the two H-O bond length of the relaxed ketonic structure are similar (2.051 Å and 2.140 Å). From the energetic analysis the most stable tautomer results to be the ketonic structure ("reference") [84]. For the ground state the energy of the single enol and double enol forms are respectively 0.60 eV and 1.26 eV above the reference. At room temperature only the ketonic form is a populated tautomer. In the first excited state the ketonic form is still the lowest energy form (excited reference) and the single enol and double enol excited forms are respectively 0.43 eV and 0.97 eV above the excited reference. ESIPT mechanism is not expected based on the energetic ordering of three tautomers, which is retained in the ground state and in the first excited state (ketonic$<$single enol$<$double enol tautomer).

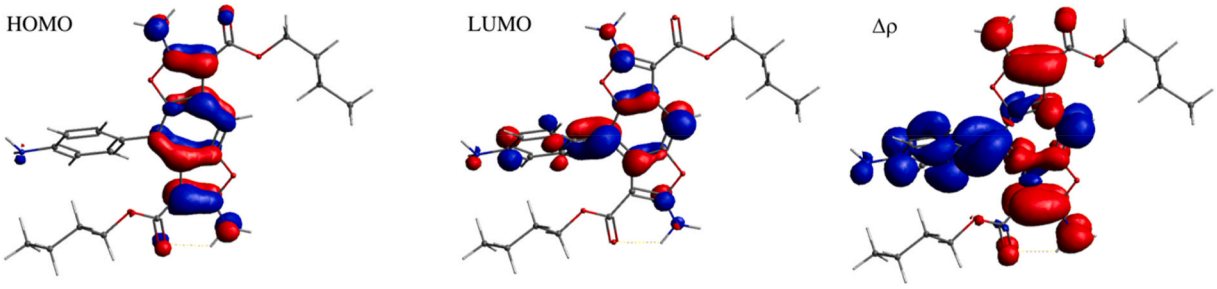

Fig. 2. HOMO (on the left) and LUMO (in the middle) orbital plot a 0.05 $|e|/a_0$ density isolevel for BDF1. Blue and red lobes represent the positive and negative sign of the wavefunction, respectively. On the right, the differential density plot (Δρ) between the first excited state and the ground state at 0.001 $|e|/a_0$ density isolevel. Blue and red surfaces are respectively positive and negative values of the difference between excited and ground densities.

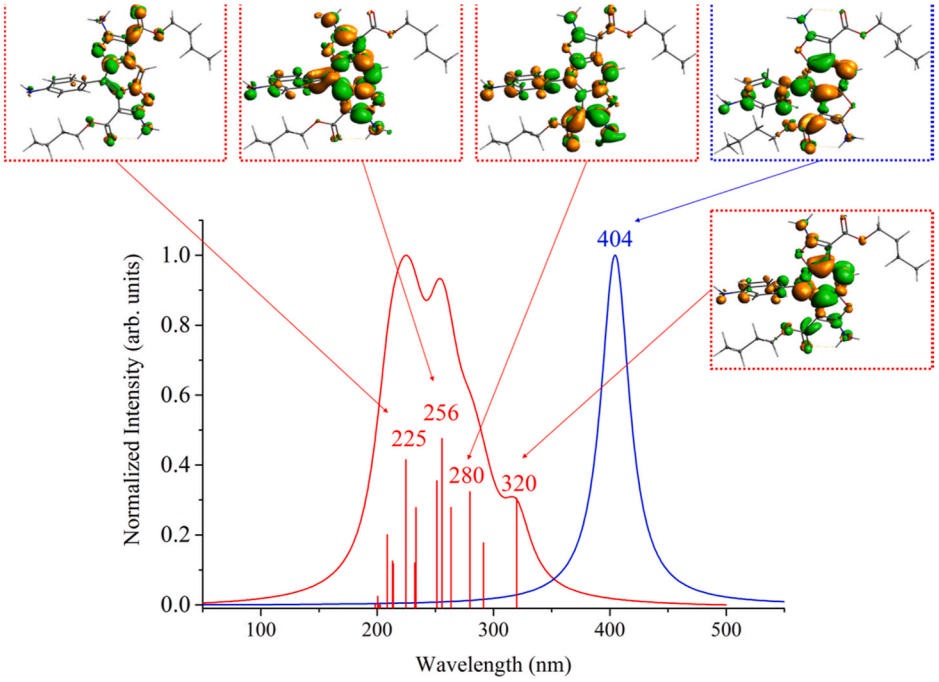

Fig. 3. Absorption (red curve) and emission (blue curve) provided by TD-DFT simulation in BDF1 system. The NTO orbital plot performed adopting 0.001 $|e|/a_0$ density isolevel are reported in dotted panels (red and blue for the absorption and emission states, respectively). In the NTO isodensities plot the green and orange lobes show the positive and negative sign of the wavefunction of each excited state.

3.3.1. HOMO-LUMO orbital analysis and NTO

The character of HOMO and LUMO of the ketonic form of BDF1 is represented in Fig. 2, where HOMO, LUMO, and orbital isosurfaces were represented at 0.05 $|e|/a_0$ density isolevel. The electron orbital in the HOMO involves the five-membered rings and the six-membered ring of the BDF core, the three amino groups, and the two hydroxyl groups. The oxygen atom groups in the furane rings are not involved in this energetic level. The LUMO isosurface involves the same atoms of the HOMO level, with the addition of the amino groups on the BDF moiety.

The electron transfer from the highest occupied level to the first unoccupied were evaluated considering the differential density Δρ between excited and ground state ($\Delta\rho = \rho^{excited}\text{-}\rho^{ground}$). This plot is an easy-to-read representation of the charge transferring in the excitation process. Δρ plot is shown in Fig. 2 at 0.001 $|e|/a_0$ isolevel. This differential density can be interpreted as an overall charge transferring from the BDF region (red lobes) of the molecule to the amino benzene region (blue lobes). This phenomenon is accompanied by a shift of the double bond's conjugation in the six membered ring of BDF with some extent of loss in conjugation. Other characterization of the HOMO=>LUMO transition through the Natural Transition Orbital formalism will be provided in the next subsection.

3.3.2. Absorption and emission spectra

From TD-DFT calculation the first 40 excitation roots (wavelength vs oscillator strength) were interpolated adopting a Lorentzian function with FWHM of 30 nm to reproduce the broad shape of the experimental data (see Fig. 3). To underline the principal component of the convolute broad band (red curve in Fig. 3), the position of the most intense peaks is reported with red bars. In the bars plot all data with normalized intensity below the cutoff value of 20% (compared the highest peak) have been overlooked. The relevant part of absorption spectrum ranges from 320 to 225 nm. The lowest energetic (HOMO=>LUMO) excitation is positioned at 320 nm (64% of the maximum intensity). Other four dominant peaks are located (sorted in descending energetic order) at 280 nm, 256 nm, and 225 nm. These peaks were analyzed in term of orbital components. It is worth of note that in the case of excited state the canonical molecular orbital representation of an electronic transition may be complicated in terms of interpretation of single occupied and empty orbital. To overcome this problem the adoption of the Natural Transition Orbitals (NTO) provides a more suitable depiction of the orbitals involved in electron excitation. This transformation is particularly adapted for the BDF1 organic chromophore, where the electronic density is extensively delocalized over the rings and there are multiple

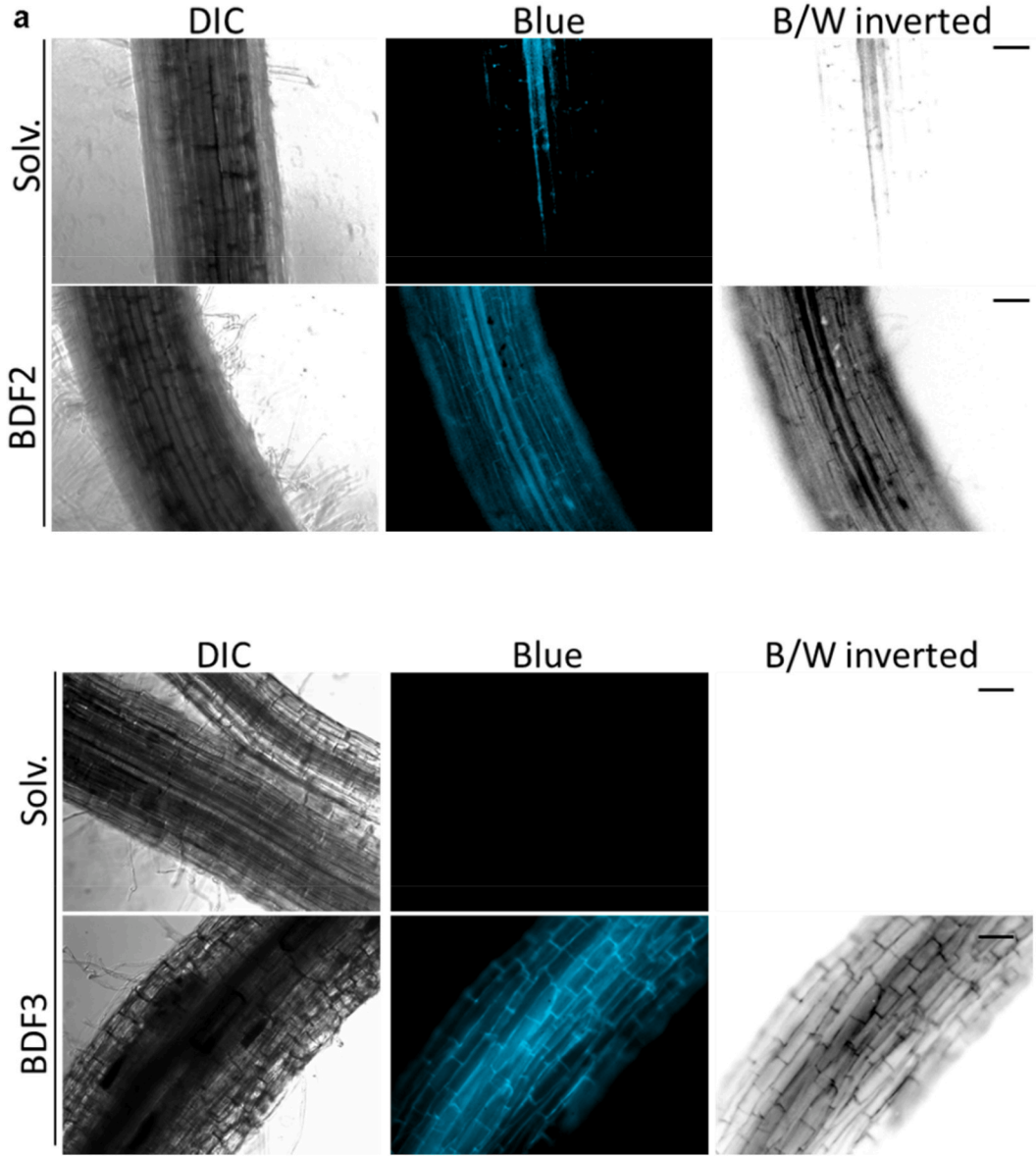

Fig. 4. Representative micrographs showing tomato root segments (1 cm long) stained with BDF2 or BDF3 and imaged through differential interface contrast (DIC) or fluorescence microscopy (blue or B/W inverted). a) Fresh tomato roots were incubated with 10 μM BDF2 dissolved in a water-based solution and imaged. Note that UV autofluorescence of the lignified xylem is visible in the control panel. b) Fresh tomato roots were cut in 1 cm long segments, incubated with 1 mM BDF3 dissolved in a glycerol-based solution and imaged. Scale bars 100 μm.

chromophoric sites. The advantage of the NTO adoption is due to the simplicity: a unitary transformation is applied to the occupied and the unoccupied set of orbitals obtaining a localized representation of the transition density matrix [85].

The NTO plot for the main excited states is reported in the red dotted mini panels in Fig. 3. The green and orange lobes represent the positive and negative sign of the wavefunction. The aim of this visual analysis provided by the orbital plots consists into underlining the main orbital components in each transition state. The orbital components are delocalized in the BDF region and involve the amino benzene ring. The orbital delocalization decreases when the energy of excited transition increase. Analyzing the molecular orbital weight of each transition (the probability amplitude coefficient c^2 of each orbital component in the single excited state), the 320 nm level is mainly ascribed to HOMO=>LUMO orbital transition (more than 94%). The main orbital components of 280 nm state are 70% HOMO=>LUMO and 27% HOMO-1=>LUMO+1. The other 3% are the minor contribution of several orbital components with negligible weight in the transition. For 256 nm and 225 nm states we find the same situation, with a 62% of contribution provided by the HOMO=>LUMO orbital transition and another 31% ascribable to HOMO-1=> LUMO+1 orbital transition. Finally, 7% are minor negligible orbital components.

The same analysis was performed for the single emission peak (blue curve at 405 nm in Fig. 2). The estimated value for the fluorescence maximum was obtained relaxing the first excited state, through the excited state gradient evaluation, following the Kasha rule [86]. This first transition level is mainly composed by LUMO=>HOMO relaxation (more than 98%) with very similar delocalized behavior in the BDF region and in the amino benzene region, also involving the amino groups. The fluorescence emission can be ascribed to the internal charge transfer (ICT) process related to the negative and positive regions. Remarkably, both adsorption and emission patterns are in good agreement with experimental data and the absorption excitation energy of BDF2 (in water CPCM [87] solvent) and BDF3 provided similar results compared to BDF1. In BDF2 we found HOMO=>LUMO excitation at 328 nm with other dominant peaks at 318 nm, 263 nm, 235 nm. For BDF3 we found

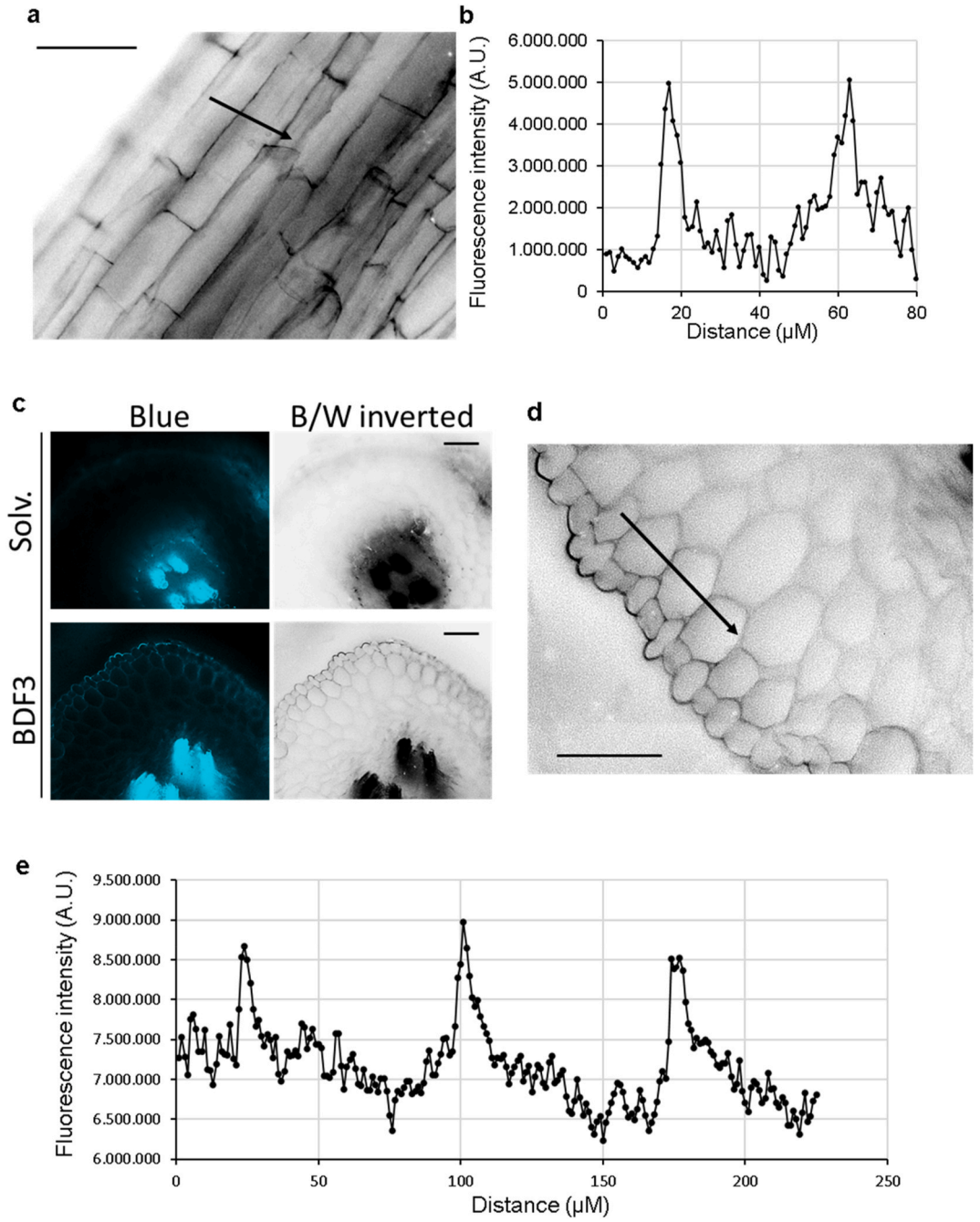

Fig. 5. Representative micrographs and intensity quantification of fluorescence signals on tomato roots stained with BDF3 and imaged through fluorescence microscopy (blue or B/W inverted). a) Close-up magnification of a 1 cm long root segment stained with 1 mM BDF3 dissolved in glycerol-based solution. b) Quantification of BDF3 signal intensity across an epidermal cell (80 μm window; black arrow) of the BDF3 stained root segment shown in a. c) Root cross-sections were incubated with 1 mM BDF3 dissolved in glycerol-based solution and imaged. d) Close-up magnification of a root cross-section stained with 1 mM BDF3 shown in c. e) Quantification of BDF3 signal intensity across the cortex (220 μm window; black arrow) of the BDF3 stained root section shown in d. Scale bars 100 μm.

HOMO=>LUMO transition at 329 nm and other four peaks at 284 nm, 264 nm, 222nm, and 216 nm.

3.4. BDF2 and BDF3 stain plant cell walls

Fluorescent visualization of plant root cell boundaries both in vivo or on fixed plant material represents a fundamental prerequisite for studying at cellular and subcellular levels both plant physiological processes and plant-microbe interaction dynamics occurring in the rhizosphere. Here, we tested the ability of BDF2 and BDF3 to stain different plant cell compartments. To this aim, we tested different concentrations of each dye, ranging from 10 μM to 1 mM, by dissolving the water-based or glycerol-based stock solutions (see Section 2.5). Interestingly, treatment of whole root mounts with both BDF2 and BDF3 resulted in an increase in plant root fluorescence compared to roots solely treated with the solvent (Fig. 4 and S5a-b). We modulated the system to obtain optimal stain concentrations (best signal-to-noise ratio) depending on both the chemical compound used (BDF2 or BDF3) and the chemical environment tested (glycerol or water). In general, the presence of a glycerol-based solution allowed to use significantly higher concentrations of both BDF2 (500 μM) and BDF3 (1mM) stains without a concomitant increase in primary fluorescence or autofluorescence of

root sections treated with the corresponding solvent control solutions (Fig. 4 and S5a-b). Indeed, roots stained with BDF2 and BDF3 compounds dissolved in a water-based solution gave sufficient signal-to-noise ratio when compared to the corresponding solvent treated samples only if used at lower concentrations (BDF2, 10 μM; BDF3, 500 μM) (Fig. 4 and S5a-b). In general, the best signal-to-noise ratio could be observed by treating tomato roots with 10 μM BDF2 in water-based solution and 1mM BDF3 in glycerol-based solution (Fig. 4).

Notably, both BDF2 and BDF3 preferentially stained plant cell walls, suggesting compound's ability to interact specifically with plant cell wall components. This was confirmed by the presence of a similar staining pattern in whole root mounts treated with the cell wall specific dye CFW (Fig. S5c). Among the two dyes, BDF3 gave a clearer resolution of individual plant root cells as its use allowed for clear visualization of epidermal or epidermal and cortex cells, respectively in whole root mounts or root cross sections (Figs. 4 and 5). Importantly, root treatment with BDF3 (dissolved in the glycerol-based fluorescence booster mixture) resulted in enhanced cell death as evidenced by discrete PI localization into plant cell nuclei (Fig. S6), likely being a result of the hyperosmotic stress resulting from the high concentrations of glycerol in which the BDF3 stain is dissolved. In accordance with this, roots treated with the corresponding solvent solution, but not those treated with a BDF2 water-based solution, leaded to similar levels of plant cell death, as evidenced by a similar PI staining pattern (Fig. S6).

All the above results suggest that both BDF2 and BDF3 might be used as efficient stains of plant root cell walls. Specifically, BDF3 staining can be preferably used on dead or fixed plant material given its higher toxicity on plant cells. On the other hand, staining with BDF2 in low-concentration aqueous solution can also be used in live microscopy approaches as it doesn't show a significant harmful effect on plant tissues.

4. Conclusions

By a facile synthetic route, we obtained three FBAs based on the same architectural core. The compounds BDF1-3 are colorless fluorophores emitting in the blue region. Unlike the common use, we designed BDF2 and BDF3 to improve the solubility in an aqueous medium and to enhance interaction with the living cell. We collected data starting from the basic chemical-physical analysis to the theoretical DFT study. Specifically, PLQYs were measured in different solvents and the influence of the pH was evaluated. The comprehensive characterization shed light on the potential use of these novel fluorescence probes as tools for imaging of fixed and alive plant tissues. The ability of BDF2 and BDF3 probes to stain different plant cell compartments was tested by providing a fluorescent visualization of plant root cell boundaries. Epifluorescence microscopy was used in a water-based solvent or in a glycerol-based solvent. Our results suggest that both BDF2 and BDF3 can be employed as efficient stains for plant root cell walls. Remarkably, BDF2 can be used for studying plant cell wall morphological and developmental stages in vivo, owing its low toxicity on living plant cells.

Funding

The authors gratefully acknowledge the financial aid provided by the Italian Ministry of Education, University and Research (MIUR), under grants PON PANDION 01_00375.

CRediT authorship contribution statement

Rosita Diana: Conceptualization, Methodology, Data curation, Writing – review & editing, Supervision. **Ugo Caruso:** Methodology, Investigation. **Francesco Silvio Gentile:** Methodology, Data curation. **Luigi Di Costanzo:** Investigation, Writing – review & editing. **David Turrà:** Investigation. **Stefania Vitale:** Investigation, All authors have read and agreed to the current version of the manuscript. **Barbara Panunzi:** Conceptualization, Writing – original draft, preparation, Writing – review & editing, Supervision, Funding acquisition.

Declaration of competing interest

The authors declare that they have no known competing financial interests or personal relationships that could have appeared to influence the work reported in this paper.

Appendix A. Supplementary data

Supplementary data to this article can be found online at https://doi.org/10.1016/j.dyepig.2021.110071.

References

[1] Munyemana JC, Chen J, Han Y, Zhang S, Qiu H. A review on optical sensors based on layered double hydroxides nanoplatforms. Microchim Acta 2021;188(3).
[2] Wu L, Liu J, Li P, Tang B, James TD. Two-photon small-molecule fluorescence-based agents for sensing, imaging, and therapy within biological systems. Chem Soc Rev 2021;50(2):702–34.
[3] From U.S. Pat. Appl. Publ. ( ) UAM Kyriazis LL, Joseph F, Lynch Peter T, Rumore Peter J, McAlpine Thomas J. Water-soluble dye compositions useful for liquid addition to various products. USA2021: US Pat Appl Publ; 2021.
[4] Jensen JD, Bisballe N, Kacenauskaite L, Thomsen MS, Chen J, Hammerich O, et al. Utilizing selective chlorination to synthesize new triangulenium dyes. J Org Chem 2021.
[5] Ershova AI, Alekseeva AU, Ershov OV, Ievlev MY, Bardasov IN. Synthesis and spectral studies of novel nicotinonitrile-based fluorescent dyes. Dyes Pigments 2022;197:109914.
[6] Eltyshev AK, Chernysheva NV, Minin AS, Pozdina VA, Slepukhin PA, Benassi E, et al. Fluorescent mesoionic 1-(2-aryl-4H-thieno[3,4-d][1,2,3]triazol-2-ium-4-ylidene)ethan-1-olates: one-pot synthesis, photophysics, and biological behavior. Dyes and Pigments; 2021.
[7] Christie RM. Pigments, dyes and fluorescent brightening agents for plastics: an overview. Polym Int 1994;34:351–61.
[8] El-Sedik M, Aysha T, Youssef Y. Synthesis, photophysical properties, and application of optical brighteners based on stilbene-oxadiazole derivatives. Color Technol 2017;133(2):122–7.
[9] Narkar N. Text Dyer Print 1979;3:56–61.
[10] Hussain M, Shamey R, Hinks D, El-Shafei A, Ali SI. Synthesis of novel stilbene-alkoxysilane fluorescent brighteners, and their performance on cotton fiber as fluorescent brightening and ultraviolet absorbing agents. Dyes Pigments 2012;92(3):1231–40.
[11] Chitcholtan K, Harris E, Yu YP, Harland C, Garrill A. An investigation into plasmolysis in the oomycete Achlya bisexualis reveals that membrane-wall attachment points are sensitive to peptides containing the sequence RGD and that cell wall deposition can occur despite retraction of the protoplast. Can J Microbiol 2012;58(10):1212–20.
[12] Bellanger AP, Millon L, Khoufache K, Rivollet D, Bièche I, Laurendeau I, et al. Aspergillus fumigatus germ tube growth and not conidia ingestion induces expression of inflammatory mediator genes in the human lung epithelial cell line A549. J Med Microbiol 2009;58(2):174–9.
[13] Zhang G, Zheng H, Guo M, Du L, Liu G, Liu J. A novel polymeric fluorescent brightener agent based on 4,4′-diamino-stilbene-2,2′-disulfonic acid-triazine structure: synthesis, characterization, photo-property, and performance on paper as light stabilizer, fluorescent brightener, and surface-sizing agent. J Wood Sci 2016;62(6):526–36.
[14] Zhang Y, Shi W, Feng D, Ma H, Liang Y, Zuo J. Application of rhodamine B thiolactone to fluorescence imaging of Hg 2+ in Arabidopsis thaliana. Sensor Actuator B Chem 2011;153(1):261–5.
[15] Bielas R, Wróbel-Marek J, Kurczyńska EU, Neugebauer D. Pyranine labeled polymer nanoparticles as fluorescent markers for cell wall staining and imaging of movement within apoplast. Sensor Actuator B Chem 2019;297.
[16] Geddes CD. Reviews in fluorescence. Springer; 2016.
[17] Goossens A, Pauwels L. Jasmonate signaling: methods and protocols. In: Methods mol. Biol. N.Y., NY, U. S.: Springer; 2013. 2013;1011.
[18] Hirsch R. Exploring colour photography: a complete Guide. 2004.
[19] Wang N, Wang L. Acid-brightening fluorescent protein (abFP) for imaging acidic vesicles and organelles. Methods Enzymol 2020:167–89.
[20] Paës G. Fluorescent probes for exploring plant cell wall deconstruction: a review. Molecules 2014;19(7):9380–402.
[21] Wallace IS, Anderson CT. Small molecule probes for plant cell wall polysaccharide imaging. Front Plant Sci 2012;3(MAY).
[22] Bidhendi AJ, Chebli Y, Geitmann A. Fluorescence visualization of cellulose and pectin in the primary plant cell wall. J Microsc 2020;278(3):164–81.
[23] Zhang B, Gao Y, Zhang L, Zhou Y. The plant cell wall: biosynthesis, construction, and functions. J Integr Plant Biol 2021;63(1):251–72.
[24] Farrokhi N, Burton RA, Brownfield L, Hrmova M, Wilson SM, Bacic A, et al. Plant cell wall biosynthesis: genetic, biochemical and functional genomics approaches to the identification of key genes. Plant Biotechno. J. 2006;4(2):145–67.

[25] Burton RA, Gidley MJ, Fincher GB. Heterogeneity in the chemistry, structure and function of plant cell walls. Nat Chem Biol 2010;6(10):724–32.
[26] Liu Z, Lavis LD, Betzig E. Imaging live-cell dynamics and structure at the single-molecule level. Mol Cell 2015;58(4):644–59.
[27] Moran-Mirabal JM. The study of cell wall structure and cellulose-cellulase interactions through fluorescence microscopy. Cellulose 2013;20(5):2291–309.
[28] Krishnamurthy KV. Methods in cell wall Cytochemistry. 6000 Broken Sound parkway NW. Suite 300 Boca Raton, FL: Taylor & Francis Group; 1999. p. 33487–42742.
[29] Hoch HC, Galvani CD, Szarowski DH, Turner JN. Two new fluorescent dyes applicable for visualization of fungal cell walls. Mycologia 2005;97(3):580–8.
[30] Ma L, Feng X, Wang S, Wang B. Recent advances in AIEgen-based luminescent metal-organic frameworks and covalent organic frameworks. Mater Chem Front 2017;1(12):2474–86.
[31] Herwig L, Rice AJ, Bedbrook CN, Zhang RK, Lignell A, Cahn JKB, et al. Directed evolution of a bright near-infrared fluorescent rhodopsin using a synthetic chromophore. Cell Chem. Biol. 2017;24(3):415–25.
[32] Khanam H, Shamsuzzaman. Bioactive Benzofuran derivatives: a review. Eur J Med Chem 2015;97(1):483–504.
[33] DeSimone RW, Currie KS, Mitchell SA, Darrow JW, Pippin DA. Privileged structures: applications in drug discovery. Comb Chem High Throughput Screen 2004;7(5):473–93.
[34] Diana R, Caruso U, Di Costanzo L, Bakayoko G, Panunzi B. A novel DR/NIR T-shaped aiegen: synthesis and x-ray crystal structure study. Crystals 2020;10(4).
[35] Carella A, Borbone F, Roviello A, Roviello G, Tuzi A, Kravinsky A, et al. Benzodifuroxazinones, a new class of heteroacene molecules for possible applications in organic electronics: synthesis, electronic properties and crystal structure. Dyes Pigments 2012;95(1):116–25.
[36] Caruso U, Panunzi B, Roviello GN, Roviello G, Tingoli M, Tuzi A. Synthesis, structure and reactivity of amino-benzodifurane derivatives. Compt Rendus Chem 2009;12(5):622–34.
[37] Alper-Hayta S, Arisoy M, Temiz-Arpaci O, Yildiz I, Aki E, Özkan S, et al. Synthesis, antimicrobial activity, pharmacophore analysis of some new 2-(substitutedphenyl/benzyl)-5-[(2-benzofuryl)carboxamido]benzoxazoles. Eur J Med Chem 2008;43(11):2568–78.
[38] Soni JN, Soman SS. Synthesis and antimicrobial evaluation of amide derivatives of benzodifuran-2-carboxylic acid. Eur J Med Chem 2014;75:77–81.
[39] Ashok D, Sudershan K, Khalilullah M. Solvent-free microwave-assisted synthesis of E-(1)-(6-benzoyl-3,5-dimethylfuro[3′,2′:4,5]benzo[b]furan-2-yl)-3-(aryl)-2-propen-1-ones and their antibacterial activity. Green Chem Lett Rev 2012;5(2):121–5.
[40] Hayakawa I, Shioya R, Agatsuma T, Furukawa H, Naruto S, Sugano Y. 4-Hydroxy-3-methyl-6-phenylbenzofuran-2-carboxylic acid ethyl ester derivatives as potent anti-tumor agents. Bioorg Med Chem Lett 2004;14(2):455–8.
[41] Xie F, Zhu H, Zhang H, Lang Q, Tang L, Huang Q, et al. In vitro and in vivo characterization of a benzofuran derivative, a potential anticancer agent, as a novel Aurora B kinase inhibitor. Eur J Med Chem 2015;89:310–9.
[42] Thévenin M, Thoret S, Grellier P, Dubois J. Synthesis of polysubstituted benzofuran derivatives as novel inhibitors of parasitic growth. Bioorg Med Chem 2013;21(17):4885–92.
[43] Feng Z, Mohapatra S, Klimko PG, Hellberg MR, May JA, Kelly C, et al. Novel benzodifuran analogs as potent 5-HT2A receptor agonists with ocular hypotensive activity. Bioorg Med Chem Lett 2007;17(11):2998–3002.
[44] Wang YN, Liu MF, Hou WZ, Xu RM, Gao J, Lu AQ, et al. Bioactive benzofuran derivatives from cortex mori radicis, and their neuroprotective and analgesic activities mediated by mGluR1. Molecules 2017;22(2).
[45] Carella A, Roviello V, Iannitti R, Palumbo R, La Manna S, Marasco D, et al. Evaluating the biological properties of synthetic 4-nitrophenyl functionalized benzofuran derivatives with telomeric DNA binding and antiproliferative activities. Int J Biol Macromol 2019;121:77–88.
[46] Huo L, Huang Y, Fan B, Guo X, Jing Y, Zhang M, et al. Synthesis of a 4,8-dialkoxy-benzo[1,2-b:4,5-b′]difuran unit and its application in photovoltaic polymer. Chem Commun 2012;48(27):3318–20.
[47] King TJ, Newall CE. 175. The chemistry of colour reactions. The craven reaction. J Chem Soc 1965:974–7.
[48] Obushak MD, Martyak RL, Matiychuk VS. Synthesis of heterocycles on the basis of arylation products of unsaturated compounds. Part 9. Dialkyl 2,6-diamino-4-arylfuro[2′,3′:4,5]benzo[b]furan-3,7-dicarboxylates from 2-aryl-1,4-benzoquinones and cyanoacetic esters. Pol J Chem 2002;76(10):1419–24.
[49] Gerszberg A, Hnatuszko-Konka K, Kowalczyk T, Kononowicz AK. Tomato (Solanum lycopersicum L.) in the service of biotechnology. Plant Cell Tissue Organ Cult 2015;120(3):881–902.
[50] Ranjan A, Ichihashi Y, Sinha NR. The tomato genome: implications for plant breeding, genomics and evolution. Genome Biol 2012;13(8).
[51] Tohge T, Scossa F, Wendenburg R, Frasse P, Balbo I, Watanabe M, et al. Exploiting natural variation in tomato to define pathway structure and metabolic regulation of fruit polyphenolics in the lycopersicum complex. Mol Plant 2020;13(7):1027–46.
[52] Chang C, Bowman JL, Meyerowitz EM. Field guide to plant model systems. Cell 2016;167(2):325–39.
[53] Johannes Schindelin IA-C, Frise Erwin, Kaynig Verena, Longair Mark, Pietzsch Tobias, Preibisch Stephan, Rueden Curtis, Saalfeld Stephan, Schmid Benjamin, Tinevez Jean-Yves, White Daniel James, Hartenstein Volker, Ptac Kevin Eliceiri. Fiji: an open-source platform for biological-image analysis. Nat Methods 2012;9:676–82.
[54] Patil VS, Padalkar VS, Tathe AB, Sekar N. ESIPT-inspired benzothiazole fluorescein: photophysics of microenvironment pH and viscosity. Dyes Pigments 2013;98(3):507–17.
[55] Dmytro A, Yushchenko VVS, Klymchenko Andrey S, Duportail Guy, Pivovarenko Vasyl G, Mély Yves. Modulation of excited-state intramolecular proton transfer by viscosity in protic media. J Phys Chem Lett 2007;111:10435–8.
[56] Lu B, Yin J, Liu C, Lin W. NIR fluorescence imaging of lipid drops viscosity in liver organs of diabetic mice. Dyes Pigments 2021:187.
[57] Kabsch W. Integration, scaling, space-group assignment and post-refinement. Acta Crystallogr Sect D Biol Crystallogr 2010;66(Pt 2):133–44.
[58] Evans PR. An introduction to data reduction: space-group determination, scaling and intensity statistics. Acta Crystallogr Sect D Biol Crystallogr 2011;67(Pt 4):282–92.
[59] Burla MC, Carrozzini B, Cascarano GL, Giacovazzo C, Polidori G. Solving proteins at non-atomic resolution by direct methods. J Appl Crystallogr 2015;48(6):1692–8.
[60] Sheldrick GM. Crystal structure refinement with SHELXL. Acta. crystal. Sec. C, Struct. chem. 2015;71(Pt 1):3–8.
[61] Farrugia LJ. WinGXandORTEP for windows: an update. J Appl Crystallogr 2012;45(4):849–54.
[62] Macrae CF, Sovago I, Cottrell SJ, Galek PTA, McCabe P, Pidcock E, et al. Mercury 4.0: from visualization to analysis, design and prediction. J Appl Crystallogr 2020;53(Pt 1):226–35.
[63] Gentile FS, Pannico M, Causà M, Mensitieri G, Di Palma G, Scherillo G, et al. Metal defects in HKUST-1 MOF revealed by vibrational spectroscopy: a combined quantum mechanical and experimental study. J Mater Chem 2020;8(21):10796–812.
[64] Panunzi B, Diana R, Concilio S, Sessa L, Tuzi A, Piotto S, et al. Fluorescence pH-dependent sensing of Zn(II)by a tripodal ligand. A comparative X-ray and DFT study. J Lumin 2019;212:200–6.
[65] Diana R, Caruso U, Di Costanzo L, Gentile FS, Panunzi B. Colorimetric recognition of multiple first-row transition metals: a single water-soluble chemosensor in acidic and basic conditions. Dyes Pigments 2021:184.
[66] Schindelin J, Arganda-Carreras I, Frise E, Kaynig V, Longair M, Pietzsch T, et al. Fiji: an open-source platform for biological-image analysis. Nat Methods 2012;9(7):676–82.
[67] Hong Y, Lam JWY, Tang BZ. Aggregation-induced emission: phenomenon, mechanism and applications. Chem Commun 2009;(29):4332–53.
[68] Borbone F, Caruso U, Causà M, Fusco S, Panunzi B, Roviello A, et al. Series of O,N,O-tridentate ligands zinc(II) complexes with high solid-state photoluminescence quantum yield. Eur J Inorg Chem 2014;(16):2695–703.
[69] Li K, Liu Y, Li Y, Feng Q, Hou H, Tang BZ. 2,5-bis(4-alkoxycarbonylphenyl)-1,4-diaryl-1,4-dihydropyrrolo[3,2-b]pyrrole (AAPP) AIEgens: tunable RIR and TICT characteristics and their multifunctional applications. Chem Sci 2017;8(10):7258–67.
[70] Caruso U, Panunzi B, Roviello A, Tuzi A. Fluorescent metallopolymers with Zn(II) in a Schiff base/phenoxide coordination environment. Inorg Chem Commun 2013;29:138–40.
[71] Diana R, Panunzi B. Zinc (Ii) and aiegens: the "clip approach" for a novel fluorophore family. a review. Molecules 2021;26(14).
[72] Mei J, Leung NLC, Kwok RTK, Lam JWY, Tang BZ. Aggregation-Induced emission: together we shine, united we soar. Chem Rev 2015;115(21):11718–940.
[73] Chen C, Fang C. Devising efficient red-shifting strategies for bioimaging: a generalizable donor-acceptor fluorophore prototype. Chem Asian J 2020;15(10):1514–23.
[74] Panunzi B, Diana R, Concilio S, Sessa L, Shikler R, Nabha S, et al. Solid-state highly efficient dr mono and poly-dicyano-phenylenevinylene fluorophores. Molecules 2018;23(7).
[75] Lakowicz JR. Solvent and environmental effects. Principles of fluorescence spectroscopy. 3 ed. Boston, MA: Springer. p. 205-235.
[76] Lakshmidevi V, PPa VA. Effect of solvent polarity on fluoroscence spectra of camphor sulphonic acid doped polyaniline. Mad. J. Anal. Sci. Instrument. 2017;2(1):21–4.
[77] Ye C, Gray V, Mårtensson J, Börjesson K. Annihilation versus excimer formation by the triplet pair in triplet-triplet annihilation photon upconversion. J Am Chem Soc 2019;141(24):9578–84.
[78] Dean JC, Zhang R, Hallani RK, Pensack RD, Sanders SN, Oblinsky DG, et al. Photophysical characterization and time-resolved spectroscopy of a anthradithiophene dimer: exploring the role of conformation in singlet fission. Phys Chem Chem Phys 2017;19(34):23162–75.
[79] Saito M, Koketsu T. Fluorescence enhancement of a bleachresistant solution for use in microfluidic devices. Opt Mater Express 2018;8(3):676–83.
[80] Muhammad N, Kryuchkova N, Dworeck T, Rodríguez-Ropero F, Fioroni M. Enhanced EGFP fluorescence emission in presence of PEG aqueous solutions and PIB1000-PEG6000-PIB1000 copolymer vesicles. BioMed Res Int 2013;2013.
[81] Padalkar VS, Seki S. Excited-state intramolecular proton-transfer (ESIPT)-inspired solid state emitters. Chem Soc Rev 2016;45(1):169–202.
[82] Yan D, Lou Y, Yang Y, Chen Z, Cai Y, Guo Z, et al. Dye-modified metal-organic framework as a recyclable luminescent sensor for nicotine determination in urine solution and living cell. ACS Appl Mater Interfaces 2019;11(50):47253–8.
[83] Huang J, Xu Y, Qian X. A red-shift colorimetric and fluorescent sensor for Cu2+ in aqueous solution: unsymmetrical 4,5-diaminonaphthalimide with N-H deprotonation induced by metal ions. Org Biomol Chem 2009;7(7):1299–303.
[84] Ling Chen P-YF, Wang Hai-Ping, Pan Mei. Excited-state intramolecular proton transfer (ESIPT) for optical sensing in solid state. Adv. Optical Mater. Adv. Optical Mater. 2021:2001952.

[85] Martin RL. Natural transition orbitals. J Chem Phys 2003;118(11):4775–7.
[86] Kasha M. Characterization of electronic transitions in complex molecules. Discuss Faraday Soc 1950;9:14–9.
[87] Barone V, Cossi M. Quantum calculation of molecular energies and energy gradients in solution by a conductor solvent model. J Phys Chem 1998;102(11):1995–2001.